Preprint Title	Impact of device design on the electronic and optoelectronic properties of integrated Ru-terpyridine complexes
Authors	Max Mennicken, Sophia K. Peter, Corinna Kaulen, Ulrich Simon and Silvia Karthäuser
Publication Date	11 Nov. 2021
Article Type	Full Research Paper
Supporting Information File 1	Ru_device_Suppinfo.pdf; 1.1 MB
ORCID® iDs	Corinna Kaulen - https://orcid.org/0000-0003-1194-5192; Silvia Karthäuser - https://orcid.org/0000-0003-3953-6980

Impact of device design on the electronic and optoelectronic properties of integrated Ru-terpyridine complexes

Max Mennicken[1,2], Sophia Katharina Peter[3], Corinna Kaulen[3,4], Ulrich Simon[3], Silvia Karthäuser[1*]

Address:

[1]Peter Grünberg Institut (PGI-7) and JARA-FIT, Forschungszentrum Jülich GmbH, Jülich 52425, Germany.

[2]RWTH Aachen University, Aachen 52062, Germany

[3]Institute of Inorganic Chemistry and JARA-FIT, RWTH Aachen University, Aachen 52074, Germany

[4]Faculty of Medical Engineering and Applied Mathematics, FH Aachen, University of Applied Science, Jülich 52428, Germany

Email:

Silvia Karthäuser* - s.karthaeuser@fz-juelich.de

*Corresponding author

Abstract

The performance of nanoelectronic and molecular electronic devices relies strongly on the employed functional units and their addressability, which is often a matter of appropriate interfaces and device design. Here, we compare two promising designs to build up solid-state electronic devices utilizing the same functional unit. Optically addressable Ru-terpyridine complexes were incorporated in supramolecular wires or employed as ligands of gold nanoparticles and contacted by nanoelectrodes. The resulting small area nanodevices were thoroughly electrically characterized as a function of temperature and light exposure. Differences in the resulting device conductance could be attributed to the device design and the respective transport mechanism: thermally activated hopping conduction in case of Ru-terpyridine wire devices or sequential tunneling in nanoparticle-based devices. Furthermore, the conductance switching of nanoparticle-based devices upon 530 nm irradiation was attributed to plasmon-induced metal-to-ligand charge-transfer in the Ru-terpyridine complexes used as switching ligands. Finally, our results reveal a superior device performance of nanoparticle-based devices compared to molecular wire devices based on Ru-terpyridine complexes as functional units.

Keywords:

1. Introduction

Discernible properties of nanoelectronic and molecular devices are directly influenced by the molecular structure of the constituting molecular systems, the intermolecular and interfacial interactions and the design of the device. Molecular engineering is requested to design and assemble molecules or supramolecular systems with specific functions and to ensure the device performance. Favorable molecular systems are capable of performing electronic operations such as data storage, rectification, sensing or switching. In this regard metallo-supramolecular wires are promising candidates as electronic and luminochromic materials and are useful in a variety of other applications [1-3]. They are available with different transition metal centers and numerous chelating ligands. The ligands may be designed to promote the wire growth, to include additional functionalities, or to form bridges to biomolecules [4,5]. Common ligands, particularly suitable for the metallo-supramolecular wire growth and exhibiting high binding constants to a broad range of transition metal ions, are often based on 2,2′:6′,2″-terpyridine (TP) motives [5-7]. In addition, TP-complexes themselves or as hybrid materials with (semi)conducting species are redox-active and thus, enable applications in nanoelectronics and catalysis [8-10]. Among the suitable transition metal centers Ru is highly attractive, since $Ru(TP)_2$-complexes reveal intense metal-to-ligand charge-transfer absorption bands and a relatively long lifetime of the triplet state as well as voltage-driven molecular switching in solid-state molecular junctions [11-15]. In addition, $Ru(TP)_2$-complexes and the corresponding supramolecular wires exhibit a rod-like structure which promotes them to be superior candidates for charge transport studies and functional nanodevices [16-18].

Using TP-based ligands and a reactive Ru precursor, we recently succeeded to establish a room-temperature method to grow Ru-TP supramolecular wires by sequential reaction [19]. The stepwise wire growth was verified by infrared reflection absorption spectroscopy and surface-enhanced Raman spectroscopy in combination with density functional theory calculations, as well as variable angle spectroscopic ellipsometry. Based on this wire formation protocol the on-chip preparation of $Ru(TP)_2$-

complex wires to bridge a nanometer sized gap between two electrodes becomes accessible. The challenge is to integrate these redox-active Ru(TP)$_2$-complex wires reliably into a device geometry so that the envisaged device properties are established. Here, our approach is to employ nanodevices equipped with nanoelectrodes separated by gaps of 8 nm to 20 nm. They are fabricated by electron beam lithography (EBL) in a lift-off process and the use of a self-aligned Al$_2$O$_3$ hard mask to define the nanogap size [20,21]. The resulting nanoelectrode pairs are used for the on-chip preparation of Ru(TP)$_2$-complex wires according to the wire-growth protocol developed recently and thus, to assemble Ru(TP)$_2$-complex wire nanodevices [19].

Additionally, we will use our already successfully applied approach to fabricate nanodevices from ligand-stabilized gold nanoparticles (AuNP) immobilized between nanoelectrodes [21-24]. Very recently, we have assembled nanodevices based on single AuNP with a diameter of 14 nm and stabilized by the twofold positively charged bis-{4'-[4-(mercaptophenyl)-2,2';6',2''-terpyridine]}-ruthenium complexes (Ru(MPTP)$_2$). A thorough electronic characterization of these single AuNP devices indicates that the redox behavior of the Ru(MPTP)$_2$-complexes is preserved in device geometry [15]. Here, we use nanodevices equipped with gaps between the nanoelectrodes in the size range of 20 nm to 50 nm so that a countable number of Ru(MPTP)$_2$–AuNP is needed to bridge the nanogaps. The thus formed Ru(MPTP)$_2$–AuNP devices are easier to fabricate and are assumed to be of higher technological relevance.

In this study, the focus of our attention lies on the relation between device design and device performance, that is, which device design is suited best to guarantee the functionality of the constituting building blocks. For this purpose, the transport properties of the redox-active Ru(TP)$_2$-complexes are studied under electrical or optical trigger in Ru(TP)$_2$-complex wire devices and in Ru(MPTP)$_2$–AuNP devices. Both devices are based on the same nanoelectrode design and are composed of analogous molecular building blocks. However, the nanogaps are bridged either directly by long Ru(TP)$_2$-complex wires or with AuNPs functionalized with TP based Ru-complexes. We will

show that it is not only a challenge to design and assemble a molecular device, but to address the constituting elements so that the device physics is mainly determined by the molecular properties.

2. Experimental methods

2.1. Chemical synthesis

4'-Mercaptophenyl-2,2':6',2"-terpyridine (MPTP), 4'-[4-(acetylthio)phenyl]-2,2':6',2"-terpyridine (MPTP-SAc), 1,4-bis(2,2':6',2"-terpyridine-4-yl)benzene (BTP), the complex $RuCl_2$(DMSO)MPTP-SAc, and the precursor [Ru(acetone)$_6$](PF$_6$)$_3$ (Ru-PF$_6$) were prepared according to procedures previously described [15,19,25-27]. The analysis of the prepared substances, including ^{1}H-NMR, UV/vis, and mass spectroscopy, display a high purity [15]. The molecular formulas of the here used chemical compounds are given in Supporting Information Figure S1.

Ru-complex functionalized AuNP were synthesized by ligand complexation of MPTP-AuNP with $RuCl_2$(DMSO)MPTP-SAc in acetic acid solution using the protocol given recently [15]. The thorough characterization revealed spherical nanoparticles, Ru(MPTP)(MPTP-SAc)-AuNP, with an average size of 14 ± 1.4 nm (Supporting Information Figure S2).

2.2. Ru(TP)$_2$-complex wire growth

For the tracking of the Ru(TP)$_2$-complex wire formation via XPS measurements mica substrates of 8 x 4 mm^2 covered by a 200 nm Au(111) layer were used. In a first step the substrates were treated with MPTP solution (1 mM in ethanol) over 24 h at RT. The Ru(TP)$_2$ wire growth was performed by (repeatedly) incubating the samples in Ru-PF$_6$ dissolved in ethanol (1 mM) over 5 min and subsequently in BTP solution (1 mM in chloroform) over 20 min at 60 °C. After each step, the samples were rinsed three times in either ethanol or chloroform.

2.3. Nanodevice fabrication

The fabrication of nanoelectrode samples, each equipped with 12 nanoelectrode pairs (consisting of an AuPd and a Pt electrode with a nanometer sized gap in between), was performed according to a process described recently using electron beam lithography and lift-off [21]. These nanoelectrode samples with gap sizes of 8 nm to 20 nm in between the electrodes were used in order to fabricate $Ru(TP)_2$-complex wire devices. According to the Ru-complex wire growth procedure described above, the samples were treated first with MPTP solution followed by alternately employing Ru-PF_6 and BTP solution.

Nanoelectrode samples with 20 to 50 nm gaps were used to assemble devices based on multiple $Ru(MPTP)_2$-AuNPs. For this purpose, a droplet of the Ru(MPTP)(MPTP-SAc)-AuNP dispersion was deposited onto the nanoelectrode structure, so that an almost complete nanoparticle layer was created. In a next step the acetyl-protected thiol groups of MPTP-SAc were hydrolyzed with concentrated ammonium solution yielding mainly $Ru(MPTP)_2$-AuNP devices, followed by a washing procedure [15]. As usual, all nanoelectrode samples have been electrically characterized before use to rule out material artifacts. Only nanogaps with a resistance > 10 TΩ were employed for further experiments. Representative SEM images of empty nanogaps, $Ru(TP)_2$-complex wire devices, and $Ru(MPTP)_2$-AuNP devices are given in Supporting Information Figure S3.

2.4. Instrumentation

X-ray photoelectron spectroscopy (XPS) measurements were conducted with a PHI5000 VersaProbe II using monochromatic Al Kα radiation (1.486 keV). Survey scans (187.5 eV pass energy, 0.8 eV/step) and core level spectra (23.5 eV pass energy, 0.1 eV/step) of the elements C 1s, N 1s, O 1s, S 1s, Ru 3d, and Au 4f were recorded. Data analysis was conducted using CasaXPS (Casa Software, Ltd.) after subtraction of a Shirley background. The binding energies (BE) were calibrated to give the signal for metallic gold Au $4f_{7/2}$ at 84.0 eV.

Scanning electron microscopy (SEM) was performed with a Hitachi SU8000 using an acceleration voltage of 5 kV.

The electronic characterization of the Ru(TP)$_2$-complex wire devices as well as the Ru(MPTP)$_2$-AuNP devices was conducted with a Keithley 6430 sub-femtoamp remote source meter as described recently [21]. Current-voltage (I/U) characteristics were taken in the temperature range from 300 K to 360 K at 1 bar pressure under helium atmosphere in an optical continuous flow cryostat (Oxford Optistat CF). Optical switching experiments were performed by applying light with the discrete wavelength in the range 440 nm to 540 nm using a Hg arc lamp and subsequent wavelength selection with monochromator (MS257 Oriel). The radiant power was 90 nW/cm^2 and the optical setup was coupled via a fiber-cable to the optical cryostat.

3. Results and Discussion

3.1. Ru(TP)$_2$-complex wire growth

Ru(TP)$_2$-complex wires were grown between electron beam lithographically fabricated nanoelectrodes according to the recently developed routine which enables the assembly of the molecular building blocks on solid surfaces at room-temperature under mild conditions and thus, represents an on-chip preparation method [19]. In parallel, the first steps of the consecutive wire growth on Au substrates were monitored by XPS measurements. The step-by-step formation of the Ru(TP)$_2$-complex wires was conducted starting with the assembly of MPTP on Au substrates, corresponding to samples (i) (Figure 1). Then the substrates were incubated in a Ru-PF$_6$ solution, leading to the formation of the Ru-MPTP half-facial complexes on the surface, representing samples (ii). Subsequently incubating the substrates in BTP solution leads to MPTP-Ru-BTP wires, corresponding to samples (iii). The wire growth was completed by incubation of samples (iii) in Ru-PF$_6$ solution for a second time, thereby forming samples (iv) (Figure 1).
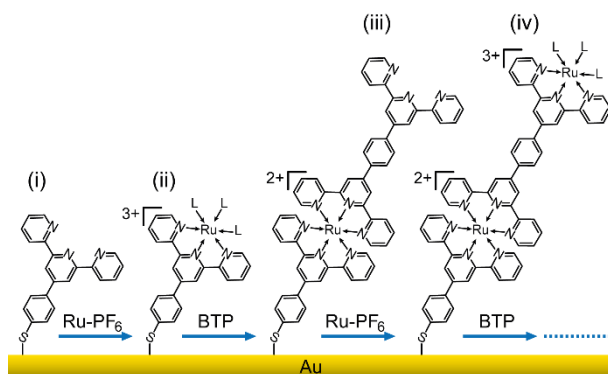
Figure 1: Stepwise Ru(TP)$_2$-complex wire growth be alternate addition of the Ru-PF$_6$ precursor in ethanol and BTP solution, (i) – (iv) see text; L = ligand (acetone or ethoxide anion).

Recently, we showed by evaluation of the IRRAS and Raman spectra of the individual wire growth steps (i) – (iii) and comparison of these spectra to the spectra of bulk model substances that the formation of the Ru(TP)$_2$-complexes was largely successful [19]. However, a detailed investigation of the oxidation state of the Ru ions bound to the respective molecular compounds is not feasible by these methods. In contrast, XPS BE are highly dependent on the oxidation state and/or the chemical composition and thus, a suitable means to reveal details of the Ru(TP)$_2$-complex wire growth process. Therefore, the core level spectra of C 1s, Ru 3d, and O 1s have been recorded after each growth step and the obtained values are given in Table 1 (see Supporting Information for in depth analysis, Section 4, and XPS core level spectra, Figure S4). Overall, the result of the detailed XPS analysis is that the wire terminating group related to the respective growth step can be readily identified by the corresponding BE for the C 1s, Ru 3d, and O 1s core levels. Growth steps (i) and (iii) characterized by a terminal TP group reveal a low intensity C 1s peak at 286.5 eV (C-N) which shifts to 286.2 eV (C-O) for growth steps (ii) and (iv) indicating a termination by the Ru(TP)(L)$_3$-complex. The related Ru 3d$_{5/2}$ peak at 282.1 eV is identified as Ru^{3+} bound to ethoxide ions for (ii) and (iv) while the Ru peak at 281.5 eV found for the MPTP-Ru-BTP wires (iii) clearly indicates Ru^{2+} corresponding to Ru(TP)$_2$-complexes [28]. Likewise, the O 1s peak assignment reveals distinctly the alternation of the terminal groups during the Ru(TP)$_2$-complex wire growth. The main O 1s peak in the spectra of sample (ii) and sample (iv) denotes the termination of

8

the wire by the Ru(TP)(L)$_3$-complex in accordance with the C 1s and Ru 3d$_{5/2}$ spectra, while the O 1s peak for growth steps (i) and (iii) points to the sporadic adsorption of ethanol to the terminal TP groups [29,30]. Thus, the XP spectra prove, in addition to earlier published results based on other spectroscopic methods, that the desired wire growth is successfully conducted and reveals the oxidation state of Ru during complex wire growth [19].

Table 1: Binding energies (in eV) of C 1s, Ru 3d$_{5/2}$, and O 1s core levels given for the consecutive wire growth steps shown in Figure 1.[a]

		C 1s			**Ru 3d$_{5/2}$**		**O 1s**		
		C-C	C-O	C-N	Ru^{2+}	Ru^{3+}	C-O$^-$	C-OH	C-OH…N
(i)	**MPTP**	**285.5**		286.7				**532.9**	534.2
(ii)	**MPTP-Ru**	**285.0**	286.2			**282.1**	**531.8**	533.0	
(iii)	**MPTP-Ru-BTP**	**284.8**		286.5	**281.5**	282.3	531.7	**532.5**	534.6
(iv)	**MPTP-Ru-BTP-Ru**	**284.9**	286.2		281.3	**282.2**	**531.4**	532.6	

[a]BE of the main peaks are given in bold letters.

3.2. Electrical properties of Ru(TP)$_2$-complex devices

Here, we study the relation between device design and device performance and compare the transport and optical switching properties of functional Ru(TP)$_2$-complexes in supramolecular wire devices and in AuNP nanodevices. Both devices are based on the same nanoelectrode design and on the identical redox-active Ru(TP)$_2$-complexes, see Figure 2. Furthermore, these devices will be compared to single Ru(MPTP)$_2$–AuNP devices described recently [15].
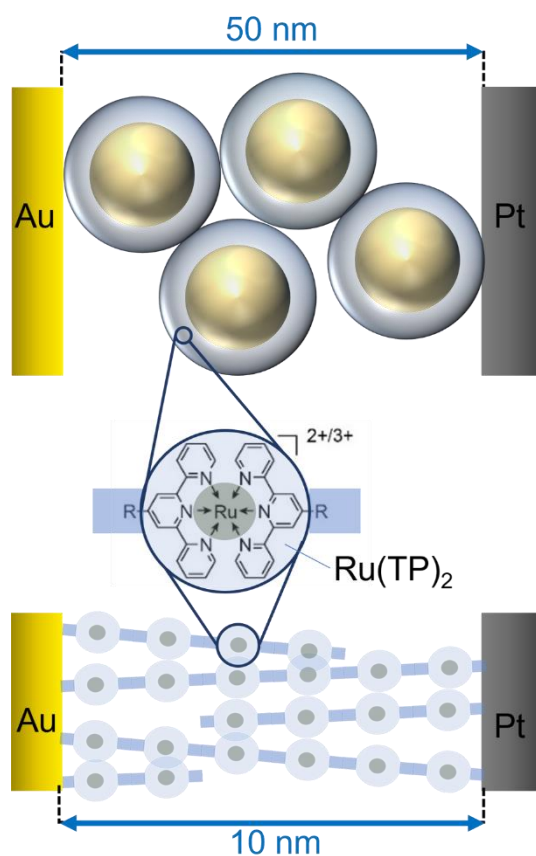
Figure 2: Schematic illustration of Ru(MPTP)$_2$–AuNP (upper part) and Ru(TP)$_2$-complex wire devices (lower left part) based on the same functional molecular unit, Ru(TP)$_2$ (not drawn to scale).

Ru(TP)$_2$-complex wire devices have been fabricated using nanoelectrodes with a separation of 8 nm to 20 nm and the above described growth process. The electrical behavior of the thus formed solid-state junctions was measured by cyclic current *versus* voltage (*I*/*U*) sweeps in the voltage range -1.3 V < *U* < +1.3 V. The resulting conductance values (at 1 V) are typically found in the range from 0.51 pS to 1.49 pS with a median of 1.35 pS and exhibit no dependence on the nanoelectrode gap size. It should be noted that reference measurements on empty nanoelectrode gaps or nanoelectrode pairs only treated repeatedly with TP solution and ethanol show conductance values around 0.01 pS, corresponding to the noise level. In Figure 3 the current *versus* voltage graph of a typical Ru(TP)$_2$-complex wire device (green) is given exhibiting a low conductance value characteristic for long supramolecular wires. These nanowire devices are compared to well accessible devices based on a few Ru(MPTP)$_2$-AuNP with a diameter of 14 nm immobilized between nanoelectrode pairs with gap sizes of 20 nm to 50 nm. Here,

the redox-active Ru(MPTP)$_2$-complexes form the ligand shell of the AuNPs. In these devices 2 to 4 Ru(MPTP)$_2$-AuNP are needed to bridge the gap between the nanoelectrodes. The AuNP devices have been characterized in the same manner as the nanowire devices. The thus determined conductance values range from 12.8 pS to 28.9 pS with a median of 16.3 pS. These values are roughly by a factor of 10 higher than the conductance values obtained for nanowire devices but three orders of magnitude lower than conductance values obtained for single AuNP devices, which can be found typically around 14 ± 3 nS. Representative conductance curves for the devices under consideration are given in Figure 3.
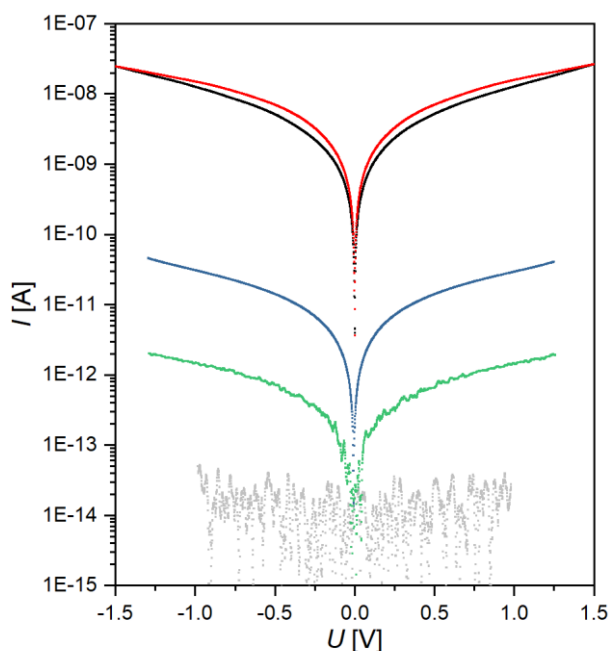

Figure 3: Log current *versus* voltage curves of Ru(TP)$_2$-complex wire devices (green), multiple Ru(MPTP)$_2$–AuNP devices (blue), single Ru(MPTP)$_2$–AuNP devices (red/black), and empty nanogaps representing the noise level (grey).

Besides the obviously different conductance values, no electrical switching could be observed for the Ru(TP)$_2$-complex wire devices and the multiple Ru(MPTP)$_2$–AuNP devices in contrast to the single Ru(MPTP)$_2$–AuNP devices. Here it should be mentioned that all our attempts to enable electrical switching in multiple Ru(MPTP)$_2$-AuNP devices by increasing the applied voltage failed in our experimental voltage window ±3 V, which is limited by the stability of the nanoelectrodes. For the

nanowire devices a rather practical reason for the missing electrical switching might be the low conductance through these devices while the expected on/off ratio of 1.5 would lead only to a minor current increase [15]. Thus, the expected electrical switching effect in these devices may be simply covered by noise. However, to discuss this issue in more detail the conductance mechanism in the different devices needs to be clarified first.

In order to determine the underlying conductance mechanism, temperature dependent measurements have been carried out. For this, the current at a constant bias of 1 V was recorded at different temperatures in the range between 293 K and 353 K. Figure 4a shows the resulting Arrhenius plot of a $Ru(TP)_2$-complex wire device. In this case the linear regression reveals an activation energy E_A = 582 meV. Over all eight samples, energies ranged from 367 meV to 584 meV with a median of 479 meV. Thus, it is reasonable to assume thermally activated hopping conduction for these solid-state devices, like it had been reported already for transition metal complex wires in solution [7,31,32]. Most interestingly, the lower limit of the activation energy determined for hopping conduction through the $Ru(TP)_2$-complex wire device corresponds well to the energy offset, $\Delta E_H = E_F - E_{HOMO}$, between the Fermi energy of the contacting electrodes and the highest occupied molecular orbital (HOMO) of the Ru-complex, which we have recently determined to 330 meV [15]. This reveals that ΔE_H is a relevant activation energy in ideal devices to be overcome for hopping conductance. In practical nanowire devices other contributions like an additional contact resistance or an activation energy for wire-to-wire hopping may become relevant, too. The absent length dependence and the distinct temperature dependence with E_A corresponding to ΔE_H point to hole conduction through the energetically accessible HOMO of $Ru(TP)_2$-complexes in solid-state nanowire devices.
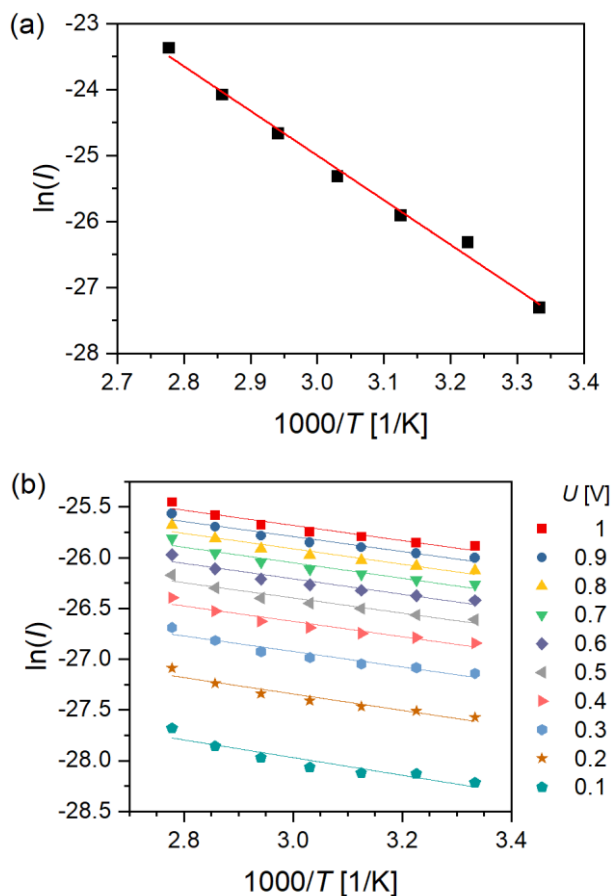
Figure 4: Arrhenius plots. (a) Ru(TP)$_2$-complex wire device (U = 1 V). (b) Ru(MPTP)$_2$–AuNP device for voltages between 0.1 V and 1 V. Points correspond to measurements while lines correspond to linear regressions.

Temperature dependent I/U measurements on Ru(MPTP)$_2$–AuNP devices are given in Figure 4b. Here, the current was measured for 10 different biases, starting with 0.1 V and increasing in 0.1 V steps up to 1 V, at each temperature. The determined activation energies are considerably smaller than those deduced for Ru(TP)$_2$-complex wire devices and decline with ascending voltage from E_A = 75 meV at 0.1 V to 64 meV at 1V (see also Supporting Information Figure S5). This small decline in E_A can be attributed to the broadening of the electron energy distribution at Fermi level and indicates a tunneling mechanism [33,34]. Tunneling mechanism has already been observed for single Ru(MPTP)$_2$-AuNP devices, as well [15]. TEM images of Ru(MPTP)$_2$-AuNP assemblies point to a nanoparticle separation of about 4 nm corresponding to slightly intercalating ligand shells or even the formation of dithiol bonds between adjacent ligand shells. Assuming a number of three Ru(MPTP)$_2$-AuNP bridging the gap

13

between the nanoelectrodes and applying the best practice to estimate the conductance for these AuNP devices a value of $G_{NP,theo}$ = 25 pS results. This value is based on sequential tunneling from AuNP to AuNP, a separation of 4 nm between the AuNP, a decay constant of β = 3.1 nm^{-1} for the Ru(MPTP)$_2$-complex (for details see Supporting Information Section 6) and fits exemplarily the experimentally obtained conductance values. Hence, the decreased conductance of the few Ru(MPTP)$_2$-AuNP device can be directly related to the changed device geometry compared to single AuNP devices, while the conductance mechanism remains tunneling transport. Thus, tunneling transport is determined for Ru-complexes bridging a gap of about 4 nm, i. e. corresponding to the distance between two AuNP, while in longer wires thermally activated hopping is the dominant transport mechanism. This finding is in notable agreement with reports from other groups [31,32,35]. Thus, the respective device design of Ru(TP)$_2$ based devices with roughly comparable dimensions in the nanometer range determines the accessible conductance values (single Ru(MPTP)$_2$-AuNP >> few Ru(MPTP)$_2$-AuNP > Ru(TP)$_2$ nanowire) and different conduction mechanisms. While single and few Ru(MPTP)$_2$-AuNP devices exhibit tunneling and sequential tunneling transport, respectively, Ru(TP)$_2$-complex wire devices exhibit hopping transport, verified by temperature dependent conductance measurements.

Next we discuss the impact of this finding on the electrical switching ability of few Ru(MPTP)$_2$-AuNP compared to single Ru(MPTP)$_2$-AuNP devices. The recently reported, ideal single AuNP devices are described as double-barrier tunnel junctions [15]. They are formed by two 2.2 nm tunneling gaps bridged by Ru(MPTP)$_2$-complexes strongly coupled to the electrodes and to the AuNP, respectively. In this scenario, a transition voltage of 1.17 eV is needed, to align the HOMO levels of the Ru-complexes with E_F of the electrodes, despite the considerably smaller energy offset between E_F and HOMO of ΔE_H = 0.33 eV. The relatively high transition voltage must be overcome to enable electrical switching of Ru$^{2+/3+}$ in this device geometry. However, in a device consisting of three AuNPs, for example (Supporting Information Section 6), in addition to single AuNP devices two tunneling gaps of 4 nm must be considered as well as strong coupling between the Ru-complexes and the AuNP but weak coupling

otherwise. Assuming tunneling transport the applied voltage will drop mainly over both 4 nm gaps leaving the HOMO levels of Ru(MPTP)$_2$-complexes in the smaller tunneling gaps almost unaffected. Thus, only a part of the orbitals relevant for a continuous conductive path from one electrode to the other is shifted into the respective voltage window defined by the measurement conditions. This kind of voltage divider, determined by the few Ru(MPTP)$_2$-AuNP device geometry, in combination with the pinning of the Ru-complex HOMO levels to the AuNPs impedes the formation of a higher conductive pathway between the electrodes, that is, a continuous path of electrically switched Ru$^{2+/3+}$. An electrical switching of only a part of the relevant Ru-complexes will have a minor effect on the device conductance if an on/off ratio = 1.5 is considered.

3.4. Optical addressing

Besides addressing the switching ability of Ru(TP)$_2$-complexes by electrical means the influence of light illumination on these Ru(TP)$_2$-complex devices is investigated. We studied the photoconductance properties of Ru(TP)$_2$ devices upon irradiation at wavelength of 490 nm to 540 nm and DC bias (U_{SD}) of 0.1 to 1.2 V (Figure 5a). Current vs. time traces were recorded while the light source was switched on and off, respectively, for a period needed until a stable current was recorded. The period was varied between 30 s and several minutes. The time evolution of the current measured for Ru(TP)$_2$ nanowire devices shows very short pulses corresponding to the light switching event. The time constant of these spike-like features could not be resolved in our measurement apparatus. However, they appear also in empty nanogap devices and therefore are attributed to plasmon excitations of the leads (see Supporting Information, Figure S7). No significant difference in the steady state current was observed for Ru(TP)$_2$-complex wire devices under illumination and in the dark (on/off ratio given in Supporting Information Figure S8).

The Ru(MPTP)$_2$-AuNP devices, consisting of 3 to 4 AuNP between the nanoelectrodes, were optically addressed by the same procedure, i. e. 530 nm irradiation (U_{SD} = 1 V) and on/off switching with

15

different frequencies (Figure 5b and Supporting Information Figure S9). Here it is possible, in contrast

to Ru(TP)$_2$-complex wire devices, to initiate conductance switching by applying an optical signal. We

find a conductance ratio of 1.03 (at 1 V) between the steady-state current under irradiation (on) and

in dark (off). This value is in line with data reported previously by us and described in literature for the

switching ratio of Ru(TP)$_2$ based monolayer devices [11,13,15].
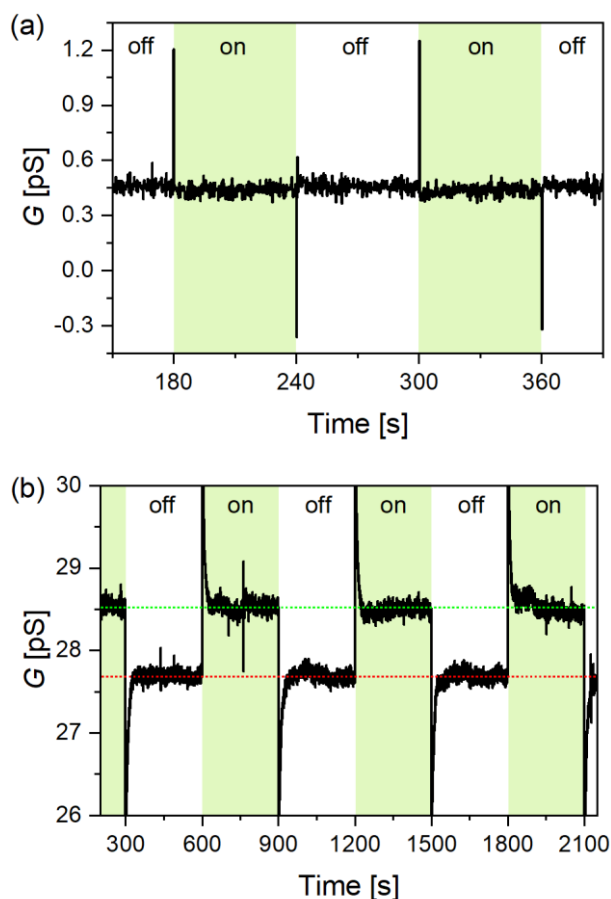
Figure 5: Current *versus* time traces at 1 V bias. Samples were illuminated with a 530 nm light. (a)
Ru(TP)$_2$-complex wire device. On/off frequency of 60 s. (b) Ru(MPTP)$_2$-AuNP device, with green and
red dotted lines indicate the steady-state conduction values. On/off frequency of 300 s.

Possible origins of this conductance switching in the Ru(MPTP)$_2$-AuNP devices should be discussed. We

can completely rule out a bolometric conductance enhancement like discussed for large nanoparticle

arrays. We address our device with 90 nW/cm^2 only to exclude this influence, in contrast to otherwise

used light intensities in the kW/cm^2 range, which are described to cause an increase in temperature of

approximately 0.55 K under certain conditions [36]. Furthermore, it is unlikely that the conductance switching in our Ru(MPTP)$_2$-AuNP devices corresponds to photoconductance as discussed for AuNP arrays consisting of AuNP coated with monolayers of organic molecules [37]. The photoconductance of these AuNP arrays is independent of U_{SD} and increases linearly with the intensity of the irradiating light, while they exhibit on/off ratios of less than 1.01 for light intensities of 1 µW/cm^2. We find an increase of the photocurrent through the Ru(MPTP)$_2$-AuNP devices due to irradiation after a threshold voltage of about 0.4 V to 0.5 V (Figure 6a). Interestingly, this value corresponds well to the range of activation energies determined above for hopping transport in Ru(TP)$_2$-complex wire devices.
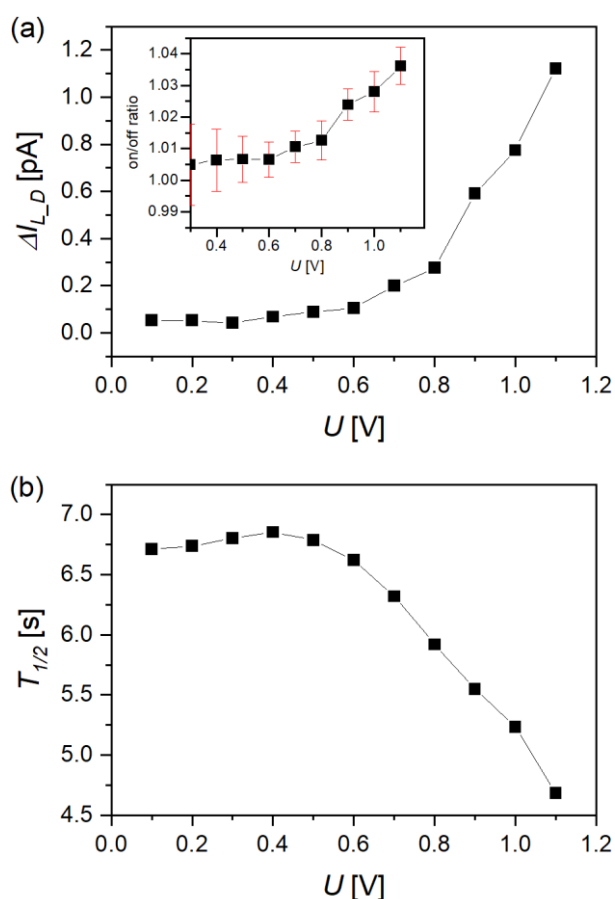
Figure 6: Photoconductance of Ru(MPTP)$_2$-AuNP devices. (a) Difference between light current and dark current, ΔI_{L_D}; inset: on/off ratio. Red bars correspond to standard deviation. (b) Half-life of current decline after peak induced by switching the light source "on" or "off".

In addition, we observe a prominent current peak in the current vs. time traces of the Ru(MPTP)$_2$-AuNP devices (Figure 5b) related to the switching on or switching off of the light source. This peak is not observed for Ru(TP)$_2$-complex wire devices. Obviously, the local surface plasmons are excited by the incident light and the oscillating electron density on the AuNP surface in the electrical field between the nanoelectrodes leads to a parasitic current which is subsequently counterbalanced by charge carriers in the nanoelectrodes. Since surface plasmon excitations are in the fs range and the diffusion of charge carriers is considerably slower, we find an exponential decay until a steady-state current is reached. The decay constant is field dependent, like expected for the motion of charge carriers (Figure 6b). In addition, the AuNP act as optical antennae, like described in literature [36-41], that is, the incident electromagnetic energy is transferred to the Ru(MPTP)$_2$-complexes bound to the AuNP surface. Such a plasmon-induced resonance energy transfer is likely, if a spectral overlap between the plasmon resonance and a molecular resonance, ideally of shorter wavelength, exists [40]. Exactly this scenario is given here: The local surface plasmon resonance of the Ru(MPTP)$_2$-AuNP is found at 533 nm while the metal-to-ligand charge transfer band of Ru(MPTP)$_2$-complexes is located at 493 nm and a considerable overlap of both bands is given [15]. Exciting the redox center of the Ru(MPTP)$_2$-complex, i. e. the Ru^{2+}-cation, creates an exciton consisting of a threefold positive Ru^{3+} and a negative charge located on the MPTP ligand. Subsequently, while applying an electrical field of sufficient energy, which is needed to initiate a hopping process, the charge carriers resulting from the plasmon-induced metal-to-ligand charge transfer are separated and contribute to the total current. Raising U_{SD} over this threshold voltage leads to a further increase in current. However, this current is strongly dependent on the number of addressable Ru(MPTP)$_2$-complexes in the ground state located between the AuNP, which is limited.

Consequently, an effective equilibrium is established between light intensity, local surface plasmons of the AuNP, Ru(MPTP)$_2$-complexes in ground state, charge carrier density, density of trap states on the AuNP cores or TP ligands, and the applied electric field. The resulting steady state current depends

on this equilibrium. The difference between the current under light illumination and the dark current, $\Delta I_{\text{L\_D}}$, corresponds to the current enabled by plasmon-induced energy transfer to the Ru(MPTP)$_2$-complexes and charge separation in an electrical field. This finding is in analogy to the plasmon-induced isomerization found in azobenzene derivatives used as ligands in nanoparticle arrays [40]. The conduction mechanism of the current contribution, $\Delta I_{\text{L\_D}}$, is assumed to be hopping conduction since the charge carriers are mainly located in the ligand shell of the AuNP. Furthermore, the activation energy for this process as well as the current range correspond well to the above described hopping transport through Ru(TP)$_2$-complex wire devices. Thus, $\Delta I_{\text{L\_D}}$ can only contribute a relatively small amount to the total current across the Ru(MPTP)$_2$-AuNP device and consequently leads to a low on/off ratio.

Since it will be difficult to increase $\Delta I_{\text{L\_D}}$, a straightforward way to improve the on/off ratio of Ru(MPTP)$_2$-AuNP devices would be to increase the distance between adjacent AuNP in the electrode gap, for example employing longer ligand molecules. This will cause a decrease of the tunneling current contribution through the device, i. e. an increase of the $\Delta I_{\text{L\_D}}$ contribution to the total current, and thus an increase of the on/off ratio. These insights indicate that Ru(TP)$_2$-complex wires are not so useful to bridge nanometer sized gaps (< 8 nm) between electrodes as single or few Ru(MPTP)$_2$-AuNP in order to build up small area functional devices. This is caused by their extremely low conductance, the missing antennae effect of AuNP in optical devices and in consequence, the absence of relevant switching currents as response to an electrical or optical trigger. Moreover, the possibilities to tune Ru(TP)$_2$-AuNP devices are more versatile.

4. Conclusion

Overall, we demonstrated that hybrid materials from Ru(TP)$_2$-complexes and AuNP integrated in CMOS compatible devices are useful switching elements that can be addressed by optical means.

Furthermore, we could show that the device performance is sensibly determined by the molecule functionality and depends strongly upon the chosen device design which can be used to define the transport mechanism. The use of long Ru(TP)$_2$-complex wires bridging 8 nm to 20 nm gaps between nanoelectrodes results in hopping conduction with a low transport efficiency and hereby the loss of significant switching ability. In a readily accessible approach using a few Ru(TP)$_2$-AuNP with a diameter of 14 nm to bridge nanoelectrode gaps of 20 nm to 50 nm a light-driven conductance switching was determined in device geometry. The underlying mechanism leading to an increase in current as response to light irradiation was identified as plasmon-induced metal-to-ligand charge-transfer in Ru(TP)$_2$-complexes and subsequent charge separation in the applied electrical field. Compared to Ru(TP)$_2$-complex nanowire devices the performance of Ru(TP)$_2$-AuNP devices is superior due to (I) the conductance mechanism based on sequential tunneling leading to a higher current, (II) the optical antennae effect of AuNP that allows to transfer energy to the functional molecules, and (III) the ease and manifoldness to adopt the properties of the constituting elements towards the requirements of the respective devices. Our results reveal that the intrinsic properties of Ru(TP)$_2$-complexes can be well preserved in Ru(TP)$_2$-AuNP devices. We are convinced that this kind of devices based on functionalized AuNP reveals the potential for the application in nanoelectronics or as sensors and we hope that our results inspire further developments in this field.

Supporting Information

The Supporting Information File includes the schemes of the chemical compounds used, SEM images of nanogaps and nanoparticles, XPS analysis performed during Ru(TP)$_2$-complex wire growth, activation energies of Ru(MPTP)$_2$-AuNP devices, a scheme for sequential tunneling in Ru(MPTP)$_2$-AuNP devices, reference measurements and additional data of optically addressed devices.

Acknowledgements

21

Funding

References

1. Winter, A.; Hoeppener, S.; Newkome, G. R.; Schubert, U. S. Adv. Mater. **2011**, 23, 3484-3498.

2. Tsukamoto, T.; Takada K.; Sakamoto, R.; Matsuoka, R.; Toyoda, R.; Maedo, H.; Yagi, T.; Nishikawa, M.; Shinjo, N.; Amano, S. et al. J. Am. Chem. Soc. **2017**, 139, 5359-5366.

3. Hammarstrom, L. Acc. Chem. Res. **2015**, 48, 840-850.

4. Giamblanco, N.; Tuccitto, N.; Zappalà, G.; Sfuncia, G.; Licciardello, A.; Marletta, G. ACS Appl. Mater. Interfaces **2015**, 7, 23353-23363.

5. Chakraborty, C.; Pandey, R. K.; Hossain, Md. D.; Futera, Z.; Moriyama, S.; Higuchi, M. ACS Appl. Mater. Interfaces **2015**, 7, 19034–19042.

6. Sakamoto, R.; Wu, K.-H.; Matsuoka, R.; Maeda, H.; Nishihara, H. Chem. Soc. Rev. **2015**, 44, 7698-7714.

7. Tuccitto, N.; Ferri, V.; Cavazzini, M.; Quici, S.; Zhavnerko, G.; Licciardello, A.; Rampi, M. A. Nature Mater. **2009**, 8, 41-46.

8. Winter, A.; Hager, M. D.; Newkome, G. R.; Schubert, U. S. Adv. Mater. **2011**, 23, 5728-5748.

9. Seo, S.; Viet, B. Q.; Hwang, E.; Cho, Y.; Lee, J.; Kawazoe, Y.; Lee, H. Small **2019**, 15, 1901183.

10. Xin, N.; Guan, J.; Zhou, C.; Chen, X.; Gu, C.; Li, Y.; Ratner, M. A.; Nitzan, A.; Stoddart, J. F.; Guo, X. Nat. Rev. Phys. **2019**, 1, 211-230.

11. Lee, J.; Chang, H.; Kim, S.; Bang, G. S.; Lee, H. Angew. Chem. **2009**, 121, 8653-8656; Angew. Chem., Int. Ed. **2009**, 48, 8501-8504.

12. Santoni, M.-P.; Nastasi, F.; Campagna, S.; Hanan, G. S.; Hasenknopf, B.; Ciofini, I. Dalton Trans. **2013**, 42, 5281-5291.

13. Seo, S.; Min, M.; Lee, J.; Lee, T.; Choi, S.-Y.; Lee, H. Angew. Chem. **2012**, 124, 112-116; Angew. Chem., Int. Ed. **2012**, 51, 108-112.

14. Schwarz, F.; Kastlunger, G.; Lissel, F.; Egler-Lucas, C.; Semenov, S. N.; Venkatesan, K.; Berke, H.; Stadler, R.; Lörtscher, E. Nature Nanotech. **2016**, 11, 170-176.

15. Mennicken, M.; Peter, S. K.; Kaulen, C.; Simon, U.; Karthäuser, S. J. Phys. Chem. C **2020**, 124, 4881-4889.

16. Li, J.-C.; Wu, J.-Z.; Gong, X. J. Phys. Chem. Lett. **2014**, 5, 1017-1021.

17. Pal, P.; Mukherjee, S.; Maity, D.; Baitalik, S. Inorg. Chem. **2018**, 57, 5743-5753.

18. Naher, M.; Bock, S.; Langtry, Z. M.; O'Malley, K. M.; Sobolev, A. N.; Skelton, B. W.; Korb, M.; Low, P. J. Organometallics **2020**, 39, 4667-4687.

19. Peter, S. K.; Kaulen, C.; Hoffmann, A.; Ogieglo, W.; Karthäuser, S.; Homberger, M.; Herres-Pawlis, S.; Simon, U. J. Phys. Chem. C **2019**, 123, 6537-6548.

20. Manheller, M.; Trellenkamp, S.; Waser, R.; Karthäuser, S. Nanotechnology **2012**, 23, 125302.

21. Mennicken, M.; Peter, S. K.; Kaulen, C.; Simon, U.; Karthäuser, S. J. Phys. Chem. C **2019**, 123, 21367-21375.

22. Manheller, M.; Karthäuser, S.; Waser, R.; Blech, K.; Simon, U. J. Phys. Chem. C **2012**, 116, 20657-20665.

23. Babajani, N.; Kowalzik, P.; Waser, R.; Homberger, M.; Kaulen, C.; Simon, U.; Karthäuser, S. J. Phys. Chem. C **2013**, 117, 22002-22009.

24. Babajani, N.; Kaulen, C.; Homberger, M.; Mennicken, M.; Waser, R.; Simon, U.; Karthäuser, S. J. Phys. Chem. C **2014**, 118, 27142–27149.

25. Fermi, A.; Bergamini, G.; Roy, M.; Gingras, M.; Ceroni, P. J. Am. Chem. Soc. **2014**, 136, 6395-6400.

26. Vaduvescu, S.; Potvin, P. G. Eur. J. Inorg. Chem. **2004**, 2004, 1763-1769.

27. Kelch, S.; Rehahn, M. Macromolecules **1999**, 32, 5818-5828.

28. Morgan, D. J. Surf. Interface Anal. **2015**, 47, 1072-1079.

29. Kerber, S. J.; Bruckner, J. J.; Wozniak, K.; Hardcastle, S. S.; Barr, T. L. J. Vac. Sci. Techn. **1996**, A14, 1314-1320.

30. Biesinger, M. C.; Lau, L. W. M.; Gerson, A. R.; Smart, R. S. C. Appl. Surf. Sci. **2010**, 257, 887-898.

31. Luo, L.; Benameur, A.; Brignou, P.; Choi, S. H.; Rigout, S.; Frisbie, C. D. J. Phys. Chem. C **2011**, 115, 19955-19961.

32. Higgins, S. J.; Nichols, R. J. Polyhedron **2018**, 140, 25-34.

33. Yuan, L.; Wang, L.; Garrigues, A. R.; Jiang, L.; Annadata, H. C.; Antonana, M. A.; Barco, E.; Nijhuis C. A. Nat. Nanotechnol. **2018**, 13, 322-329.

34. Smith, C. E.; Xie, Z.; Baldea, I.; Frisbie, C. D. Nanoscale **2018**, 10, 964-975.

35. Tefashe, U. M.; Van Nguyen, Q.; Lafolet, F.; Lacroix, J.-C.; McCreery, R. L. J. Am. Chem. Soc. **2017**, 139, 7436-7439.

36. Mangold, M. A.; Weiss, C.; Calame, M.; Holleitner, A. W. Appl. Phys. Lett. **2009**, 94, 161104.

37. Nakanishi, H.; Bishop, K. J.; Kowalczyk, B.; Nitzan, A.; Weiss, E. A.; Tretiakov, K. V.; Apodaca, M. M.; Klajn, R.; Stoddart, J. F.; Grzybowski, B. A. Nature **2009**, 460, 371-375.

38. Banerjee, P.; Conklin, D.; Nanayakkara, S.; Park, T.-H.; Therien, M. J.; Bonnell, D. A. ACS Nano **2010**, 4, 1019-1025.

39. Mangold, M. A.; Calame, M.; Mayor, M. Holleitner, A. W. J. Am. Chem. Soc. **2011**, 133, 12185-12191.

40. Stiévenard, D.; Guérin, D.; Lenfant, S.; Lévêque, G.; Nijhuis, C. A.; Vuillaume, D. Nanoscale **2018**, 10, 23122-23130.

41. Shabaninezhad, M.; Abuhagr, A.; Sakthivel, N. A.; Kumara, C.; Dass, A.; Kwak, K.; Pyo, K.; Lee, D.; Ramakrishna, G. J. Phys. Chem. C **2019**, 123, 13344-13353.